Catalysis Science & Technology

Characterization of Flame Synthesized Pd-TiO_2 Nanocomposite Catalysts for Oxygen Removal from CO_2-rich Streams in Oxy Combustion Exhausts

Journal:	*Catalysis Science & Technology*
Manuscript ID	CY-ART-01-2021-000133.R1
Article Type:	Paper
Date Submitted by the Author:	24-May-2021
Complete List of Authors:	Jung, Sungyoon; Washington University in St Louis, Energy, Environmental and Chemical Engineering Reed, Nathan; Washington University in St Louis, Energy, Environmental and Chemical Engineering Yablonsky, Gregory; Washington University in St Louis, Energy, Environmental and Chemical Engineering Biswas, Pratim; Washington University in St Louis, Energy, Environmental and Chemical Engineering

ARTICLE

Characterization of Flame Synthesized Pd-TiO_2 Nanocomposite Catalysts for Oxygen Removal from CO_2-rich Streams in Oxy Combustion Exhausts

Received 00th January 20xx,
Accepted 00th January 20xx

DOI: 10.1039/x0xx00000x

Sungyoon Jung,[a] Nathan Reed,[a] Gregory Yablonsky [a] and Pratim Biswas*[a]

Pd-TiO_2 catalysts with five Pd loadings were synthesized using a flame aerosol reactor. Studies of the initial and spent catalysts demonstrate that Pd loading impacted the size of Pd sub-nano clusters/nanoparticles and the fraction of Pd (metallic Pd, PdO, PdO_x). Increased size of Pd on catalysts' surface due to sintering, and the reduction of PdO to metallic Pd and/or PdO_x were observed during the reaction. Fractions of the total surface area of different Pd species and correlations to the apparent reaction rate constants were evaluated. Apparent kinetic constants are linearly proportional to fractions of total surface areas of metallic Pd and/or reduced Pd oxide, representing the intrinsic active site. The linear correlation between the O_2 reaction rate and the CO_2 concentration in the initial gas stream was also observed exhibiting the possible autocatalytic effect or a surface coverage effect.

Introduction

The emission of CO_2 from fossil fuel combustion in power plants is one of the dominating contributors to global warming. Oxy combustion is a promising technique that has improved combustion efficiency and produces a flue gas with a high concentration of CO_2, which can be effectively captured.[1, 2] The captured CO_2 can be either sequestered[3] or reused for enhanced oil recovery (EOR).[4] Although a high concentration of CO_2 (~63%) in the flue gas can be achieved, it cannot be directly applied for EOR or sequestration because the residual concentration of O_2 (~3%) is higher than the requirement for EOR (<100 ppmv).[5] Therefore, O_2 must be removed from the flue gas before reuse.

Catalytic O_2 removal with hydrocarbons is one promising solution. Up until now, studies have focused on catalytic CH_4 combustion for generating energy in gas turbine combustors, and on using metal doped catalysts to decrease emissions.[6-8] There has been progress toward effective CH_4 oxidation at low temperature (<773 K) and considerable work in studies of this system at different compositions, temperatures, and pressures over different metal doped catalysts.[7, 9] However, there is a significant difference between prior catalytic CH_4 combustion studies and this work. Most previous studies on catalytic CH_4 combustion used a relatively high O_2 concentration with N_2 or He, as the balance of the gas, or relatively low concentrations of CO_2 (<20%) to investigate their effects on the reaction. The challenge of this work is to decrease oxygen levels in low concentration O_2 streams (from 3% to less than 100 ppmv) in a highly concentrated CO_2 stream. Recent studies have shown the catalytic O_2 removal with CH_4 as a promising technique and reported high O_2 conversions (>95%) by using noble metal doped catalysts.[10, 11] Even though high O_2 conversion was achieved, two important aspects affecting the catalytic activity for O_2 removal were not fully investigated. First, active sites of the catalysts were not clearly elucidated. Noble metals are known to have high catalytic activity for various applications.[7, 12] However, there is still an ongoing debate on the active phase of noble metals for catalytic performance. The catalytic CH_4 combustion with noble metal supported catalysts strongly depends on the oxidation state of noble metal: Schmal et al.[12] reported that the coexistence of PdO and $PdO^{\delta+}$ played a crucial role in the enhanced CH_4 combustion. Yang et al.[13] showed that $Pd0/PdO_x$ ($0<x\leq1$) was the active phase for CH_4 combustion. Recently, Murata et al.[14] revealed mixed Pd/PdO phases to be active for the reaction. To design a catalyst with higher catalytic activity for O_2 removal, it is necessary to fully understand the active phase of noble metal. Second, the effect of excess CO_2 in the initial gas stream on the catalytic performance for O_2 removal has not been explored. Therefore, additional efforts are required to develop effective O_2 removal from oxy combustion systems.

Metal oxide catalysts doped by noble metals have been extensively researched for oxidation studies.[7, 15] To synthesize these catalysts, several methods, e.g., wet impregnation, sol-gel, and precipitation, have been widely utilized. However, these methods require additional processes, such as drying and calcination.[16] Unlike these methods, flame synthesis is a continuous one-step process.[17] Furthermore, many researchers have reported higher catalytic activity of flame-made catalysts due to their excellent dispersion of metal clusters on a metal oxide support.[18, 19] Recently, Fujiwara et al.[20] synthesized sub-nano scale metal clusters on a metal oxide support by controlling the residence time in a flame and reported a much higher fraction of metal atoms on the catalyst surface and

[a] Department of Energy, Environmental and Chemical Engineering, Washington University in St. Louis, St. Louis, MO 63130, USA. E-mail: pbiswas@miami.edu
Current affiliation: University of Miami

†Electronic Supplementary Information (ESI) available.
See DOI: 10.1039/x0xx00000x

strong metal-support interaction, both of which enhanced the catalytic activity. Also, Wang et al.[21] developed size-controlled Pt (<2 nm) doped TiO_2 films and found that the size of the Pt particles plays a crucial role in CO_2 photoreduction. Niu et al.[18] synthesized a well-dispersed Pd doped TiO_2 catalyst by using a premixed stagnation swirl flame and obtained an enhanced efficiency of CH_4 combustion compared to the one synthesized via a wet impregnation method. These previous studies demonstrated a promising application of the catalyst by an aerosol route for an effective O_2 removal via the CH_4 combustion reaction. However, despite these studies, there is still insufficient information about the fate of the nanoparticle catalysts and its correlation to the active phase of materials during the oxidation reaction.

In this study, Pd-TiO_2 catalysts were synthesized by using a diffusion flame aerosol reactor. A detailed evaluation of kinetic characteristics of the synthesized catalysts for O_2 removal were conducted. Pd-TiO_2 catalysts were synthesized with five different Pd loadings to investigate their catalytic properties. The properties of the catalyst after reaction (spent catalyst) were also investigated. The total surface area of different Pd species (metallic Pd, PdO and PdO_x ($0<x<1$)) in the as-prepared and the spent catalysts was calculated for every loading, and the relationship between the fraction of the total surface area of different Pd species and apparent reaction rate constant was established. In kinetic experiments, the effect of different initial gas compositions on O_2 removal was investigated. The goal of this paper is to develop an efficient correlation between structural characteristics and steady-state kinetic characteristics that characterize the prepared catalysts. This relationship can be used as an important tool for primary kinetic characteristics of the catalyst and further catalyst design.

Experimental section

The synthesis method is described first, followed by characterization methods, and finally, a test plan is presented.

Synthesis of Pd-TiO_2 catalysts using a flame aerosol reactor (FLAR)

The experimental setup for synthesizing Pd-TiO_2 catalysts is shown in Fig. S1a and described in previous study by Tiwari et al.[17] Briefly, titanium tetra-isopropoxide (TTIP, 99.7%, Sigma-Aldrich) and Palladium acetylacetonate ($Pd(acac)_2$, 97%, Sigma-Aldrich) were used as a support and a dopant precursor. TTIP vapor and Pd precursor droplets were generated by a bubbler and a three-jet Collison nebulizer and then, introduced into a central port of a diffusion flame burner. CH_4 and O_2 were introduced through the second and the outer port of the burner, respectively, with flow rates of 0.35 L min-1 and 2.5 L min^{-1}. In this study, five different Pd-TiO_2 catalysts were synthesized by controlling the concentration of the Pd precursor solutions (0.5 mM ~3.0 mM). The synthesized catalysts were collected using an isopore membrane filter. Details are illustrated in Supporting Information.

Characterization of synthesized and spent Pd-TiO_2 catalysts

The elemental analysis was conducted by both inductively coupled plasma mass spectroscopy (ICP-MS, Elan DRC ii, PerkinElmer) and field scanning electron microscopy (FESEM, JEOL 7001LVF FE-SEM, JEOL Ltd.) coupled with energy disperse X-ray spectroscopy (EDS). X-ray diffraction (XRD, Bruker d8 advance, Bruker) was utilized to investigate the crystallinity of the synthesized Pd-TiO_2 catalysts by using CuKα radiation (λ = 1.5418 Å) and a step size of 0.02°. The morphology and size of the synthesized catalysts were determined by scanning transmission electron microscopy (STEM) (TEM, JEOL 2100F, Jeol) coupled with energy disperse X-ray spectroscopy (EDS). The oxidation state of Pd was evaluated by X-ray photoelectron spectroscopy (XPS, Versa probe ii, Physical Electronics). Analyses for ICP-MS, XRD, and XPS were performed in triplicate. FESEM-EDS and STEM analyzed more than 150 spots for representative data.

To investigate the changes in the structural properties during the reaction, catalysts were collected after the tests. It has been reported that the structural properties of the catalyst were changed as the temperature was increased during the reaction.[18, 22] Pd nanoparticles, especially smaller than 3 nm, are sintered on a support under the methane oxidation reaction due to Ostwald ripening,[18, 23] and the sintering of nanoparticles could be accelerated with the existence of H_2O,[24, 25] which is a product of the oxygen removal reaction in this study. According to the preliminary data, a maximum O_2 conversion was obtained at near 773 K and the plateau was also reached. Therefore, 773 K was chosen as the standard temperature in this study. Hereafter the collected samples after the tests are denoted as spent catalysts. They were further characterized by using the same analytical tools mentioned above.

Experimental setup and procedure

Fig. S1b shows a differential fixed-bed reactor system. The feed gases are supplied from gas cylinders, and the gas composition is controlled by mass flow controllers. The differential fixed-bed reactor has three indentations in the middle to hold catalysts with glass fiber. Due to the low flowrate (~ 3 mL min^{-1}), the glass fiber supports the catalyst well. A thermometer and temperature controller (Econo Temperature Controller, ACE Glass Inc.) are used for temperature control. To perform an experiment, 10 mg of the catalyst was loaded into the reactor. The experiment was conducted at temperatures ranging between 298 K and 773 K and under atmospheric pressure. The gas feed stream consisted of O_2 and CH_4 in balance CO_2, with a total flow rate of 3.2 mL min^{-1}. In this study, three different CO_2 concentrations (i.e., 0%, 53%, and 95% in balance He), and three different ratios between O_2 and CH_4 concentrations (i.e., O_2 rich composition: $O_2/CH_4 \cong 2.4$, stoichiometric composition: $O_2/CH_4 \cong 2.0$, O_2 lean composition: $O_2/CH_4 \cong 1.6$) were used. The concentration of CH_4 was fixed at around 1.45%. The compositions of the gas streams were sampled through an automatic gas valve and measured by gas chromatography (GC, 7890B, Agilent Technologies, Inc.), using helium as a carrier gas. The GC was equipped with a porous layer open tubular (PLOT) capillary column (Supelco Carboxen-1010) and a thermal conductivity detector (TCD).

Results and discussion

Flame synthesis of the catalysts and their structures' characterization

During the synthesis process, TTIP vapors generated from the bubbler and Pd precursor acetylacetonate salts decompose at the different temperature regions in the flame.[17] In the lower

temperature region of the flame, TTIP vapors first form TiO_2 monomers, which subsequently undergo particle growth by collision, coalescence, and sintering. In the higher temperature region of the flame, Pd acetylacetonate salts decompose to form Pd vapor molecules, which can either condense or nucleate and subsequently be deposited on the surface of the created TiO_2 nanoparticles.[17] The condensed or deposited Pd molecules on the surface further diffuse and coalesce.[20] Varying the Pd concentrations can change the possibility of colliding with other molecules on the surface, which results in different sizes of Pd clusters/particles on the TiO_2 surface, and a previous study reported increasing sizes of Pd clusters on the TiO_2 surface with increasing Pd loading.[20] Also, under the flame synthesis conditions, different Pd species (e.g., metallic Pd and PdO) can be expected. At high temperature, some oxidation of Pd can occur due to the presence of excess oxygen.[23] For the same residence time in the flame, the oxidation extent of metal might depend on the metal concentration. In this study, five different Pd-TiO_2 catalysts were synthesized by varying the concentration of Pd precursor solution from 0.5 mM to 3.0 mM. The synthesized Pd-TiO_2 catalysts were characterized by different analytical tools, as described below.

Determining Pd loadings (ICP-MS and FESEM-EDS). ICP-MS confirmed the existence of Pd in the Pd-TiO_2 catalysts, and the specific Pd loading was determined by the same instrument (Table 1). The Pd loading values (wt%) obtained from ICP-MS increased with increasing concentrations of Pd precursor solution. It is worth noting that similar Pd loadings were obtained by FESEM-EDS, which reveals that most Pd particles were distributed on the catalyst surface, not in the bulk structure. As addressed in above section, TiO_2 and Pd precursors have different decomposition temperatures, and thereby, they are created in the different temperature regions during the flame synthesis.[17] The STEM-EDS mapping image (Fig. S2†) supports the hypothesis that the Pd nanoparticles are on the TiO_2 particle surface, which is consistent with the previous study.[17] It should be also noted that the spent catalysts showed similar Pd loadings (Table S1†), which implies that most Pd particles were still dispersed on the catalyst surface. The values obtained by ICP-MS were used for clarification of catalysts and further calculations. The five different Pd-TiO_2 catalysts are hereafter denoted as catalyst 1 (0.24 wt% Pd), catalyst 2 (0.45 wt% Pd), catalyst 3 (0.76 wt% Pd), catalyst 4 (1.08 wt% Pd), and catalyst 5 (1.25 wt% Pd), respectively. Based on the ICP-MS analytical results, the total Pd masses in 10 mg of Pd-TiO_2 catalyst ($M_{Total\ Pd}$), the mass used for all experiments, were calculated (10,000 (μg) × Total Pd loading (wt%)/100) and are shown in Table 1. As the concentrations of Pd precursor solution are increased, $M_{Total\ Pd}$ also increases, from 23.98 μg to 125.25 μg.

Distinguishing crystallinities of the catalysts and phase transformation (XRD). The crystal structures of the synthesized fresh and the spent Pd-TiO_2 catalysts were evaluated by XRD, and Fig. 1 shows their XRD spectra in the 2θ range of 20° to 60°. In the case of the fresh catalysts, a distinct peak of anatase (101) TiO_2 was obtained at a 2θ angle of 25.3°, and low-intensity of anatase (004), anatase (200), and anatase (211) peaks were observed at 2θ angles of 37.8°, 48.1°, and 55.1°, respectively. The XRD patterns revealed that the fresh catalysts have only TiO_2 anatase crystal structure, which correlates well with the JCPDS patterns of anatase (00-021-1272). In addition, the peak intensities for all crystal structures of Pd-TiO_2 catalysts were very similar to each other and similar to that of the pristine TiO_2 catalyst, which indicates that the addition of Pd did not change the crystal structure of the TiO_2. On the other hand, distinct peaks for Pd metal and PdO were not observed, which might be due to the extremely low Pd loading or to the very small sizes of the Pd clusters/particles.

In the case of the spent catalysts, distinct peaks of anatase and rutile TiO_2 were obtained like the fresh catalysts. In addition to these anatase peaks, low-intensity of rutile (110) and rutile (101) peaks were obtained at a 2θ angle of 27.3° and 36.1°, respectively, which match with rutile phase of TiO_2 (JCPDS 75-1753). A small peak was observed at approximately 54.2° which may be defined as anatase (105) TiO_2 or rutile (211) TiO_2 or Ti_2O_3 (116) referring to the JCPDS 00-021-1272, JCPDS 88-1175 and JCPDS 10-0063. In this study, this peak is more likely Ti_2O_3 (116) because there was no or much less intensity of the peak at near 54.2° was observed with fresh catalysts (Fig. 1a). This observation could be explained by the thermal transformation of the anatase phase of TiO_2 to Ti_2O_3[24] and could be supported by XPS analytical results (Section of Distinguishing oxidation states of components in fresh and spent catalysts (XPS), Fig. S5†). In Fig. 1b, all spent catalysts showed the peaks at the same 2θ angles, which indicates that they contain the mixed crystalline structures of TiO_2 (anatase and rutile) and Ti_2O_3. However, the intensities of the observed peaks were different. To clearly see the

Table 1 Total Pd loading, total Pd mass in 10 mg of Pd-TiO_2 catalyst ($M_{Total\ Pd}$), and the average size of Pd-TiO_2 particle ($d_{av,Pd-TiO_2}$), and the average size of Pd subnano-cluster/nanoparticle ($d_{av,Pd}$) as determined from ICP-MS, FESEM-EDS and STEM analyses

	Pd precursor feed concentration (mM)	Total Pd loading[a] (wt%)	Total Pd loading[b] (wt%)	$M_{Total\ Pd}$ (μg)	$d_{av,Pd-TiO_2}$ (nm)[c]	$d_{av,Pd}$ (nm)[c]
catalyst 1	0.5	0.24	0.21	23.98	7.57 ± 2.19	<0.5
catalyst 2	1.0	0.45	0.44	45.30	7.18 ± 2.07	0.51 ± 0.12
catalyst 3	1.3	0.76	0.75	75.96	7.61 ± 2.11	0.66 ± 0.16
catalyst 4	2.1	1.08	1.00	107.91	7.14 ± 1.04	0.85 ± 0.17
catalyst 5	3.0	1.25	1.25	125.25	7.34 ± 1.91	1.04 ± 0.18

[a] Total Pd loading was determined by ICP-MS.

[b] Total Pd loading was determined by FESEM-EDS.

[c] Sizes were determined by STEM (see Fig. 2).

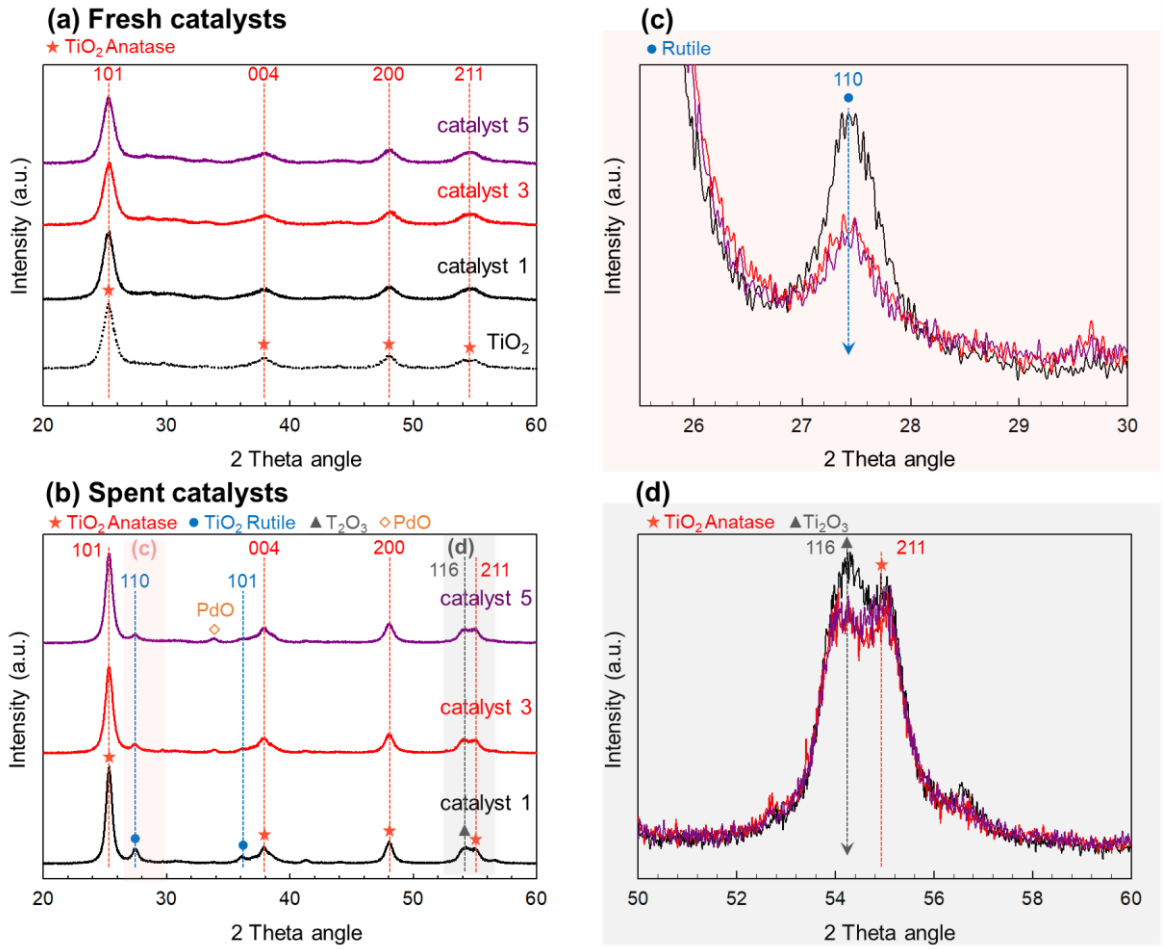

Fig. 1 XRD patterns of a) fresh catalysts and b-d) spent catalysts.

differences, two magnified versions of figures are shown in Fig. 1c (the pink-colored region at a 2θ angle ranging from 25.5° to 30° in Fig. 1b) and Fig. 1d (the grey-colored region at a 2θ angle ranging from 50° to 60° in Fig. 1b). It can be noted that the intensities of peaks of rutile (110) and Ti_2O_3 (116) were decreased as the Pd loading was increased from catalyst 1 to catalyst 5, while the peak intensity of anatase did not change much. Based on the obtained results, the intensity ratios between anatase (101) (I_{A101}, the strongest peak of anatase) and rutile (110) (I_{R110}, the strongest peak of rutile) and between I_{A101} and Ti_2O_3 (116) ($I_{Ti2O3116}$) were calculated. The calculated intensity ratio between I_{A101} and I_{R110} was decreased from 0.168 to 0.112 as the Pd loading was increased from catalyst 1 to catalyst 5. The calculated intensity ratio between I_{A101} and $I_{Ti2O3116}$ also showed the same decreasing trend from 0.184 to 0.166 with increasing the Pd loading. The previous study by Tiwari et al.[17] reported that the phase transformation of TiO_2 can be suppressed under a high temperature condition by incorporating a noble metal dopant due to its surface modification. Our current result was consistent with this previous study. On the other hand, the low-intensity peak of PdO was observed with the spent catalyst 5. This sudden appearance of PdO in spent catalyst 5 can be attributed to the sintering effect of Pd on the TiO_2 surface, which will be discussed more in the following sections.

Investigating similarities and differences of morphology and size of Pd and Pd-TiO_2 between fresh and spent catalysts (STEM). The surface morphology and size of the fresh and spent Pd-TiO_2 catalysts were investigated by STEM (Fig. 2 and all images found in Fig. S3†). In each case, we counted more than 200 particles to evaluate the particle size distribution of the Pd-TiO_2 particles, and the results are shown in the first column of Fig. 2 and in Table 1. In the case of the fresh catalyst, the Pd-TiO_2 catalysts had similar size distributions of their bulk structure, and similar average particle sizes ($d_{av,Pd-TiO_2}$, approximately 7 nm) (red-colored bars in the first column of Fig. 2) (Table 1). The fresh catalysts also had similar spherical shapes. These results reveal that the addition of Pd did not change the particle morphology and size of the bulk structures. It was confirmed that there were no noticeable Pd subnano-clusters at the lowest Pd loading (catalyst 1) (Fig. S3a†). On the other hand, extremely small Pd subnano-clusters/nanoparticles (bright dots in the yellow circles in the second column of Fig. 2), were observed. To confirm the existence of Pd subnano-clusters and nanoparticles, EDS mapping was performed with the fresh catalyst 4 (Fig. S2†) and it shows uniformly distributed Pd subnano-clusters and nanoparticles on TiO_2 surface. Pd subnano-clusters (<1 nm) were detected in catalysts 2 and 3, while both Pd subnano-clusters and Pd nanoparticles (>1 nm) were observed in catalysts 4 and 5 (Table 1). The size distributions of Pd subnano-clusters/nanoparticles in all cases were evaluated, and the results are shown with red-colored bars in the fourth column of

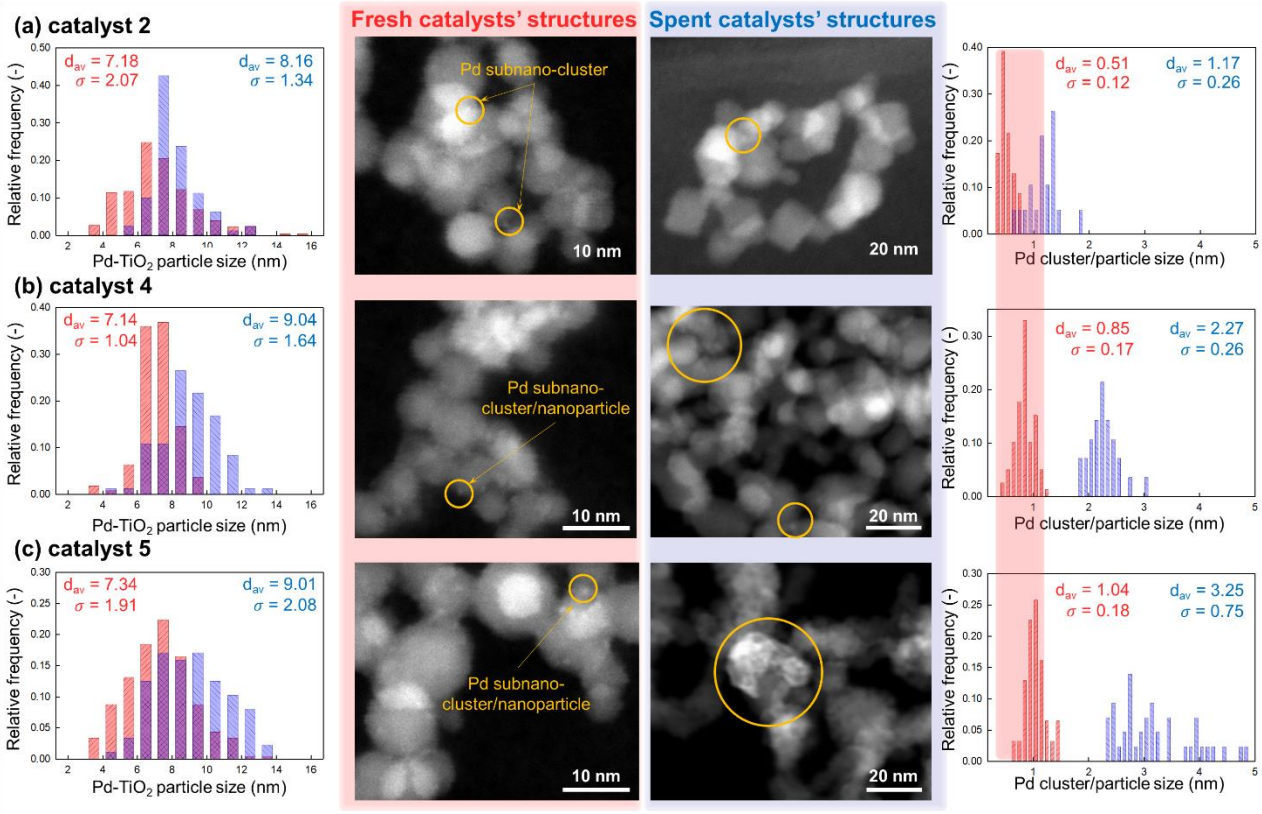

Fig. 2 Bulk Pd-TiO_2 nano particle and Pd subnano-cluster/nano particle size distributions, and STEM images of a) catalyst 2, b) catalyst 4, and c) catalyst 5. Results related to the fresh catalysts are denoted with red-color and results related to the spent catalysts are shown with blue-color.

Fig. 3 and in Table 1. The average size of Pd subnano-clusters/nanoparticles ($d_{av,Pd}$) increased with increasing Pd loading, which demonstrates that Pd loading affects the size of Pd subnano-clusters/nanoparticles on the TiO_2 surface.

In the case of the spent catalysts, the average particle sizes of Pd-TiO_2 were slightly increased to ~9 nm with the Pd loading was increased (blue-colored bars in the first column of Fig. 2). The result shows that the sintering of the Pd-TiO_2 was not severe at the high temperature condition. Compared to the fresh catalysts, the spent catalysts showed larger nanoparticles and their average sizes were increased as the Pd loading was increased. Previous studies have reported the increased size of dopants on the support materials under methane oxidation reaction due to Ostwald ripening,[18, 22, 23] and it could be accelerated with the existence of H_2O,[24, 25] which is a product of the oxygen removal reaction in this study. Our observation showed a similar trend. It is interesting to note that the spent catalyst 5 contains aggregates of Pd nanoparticles on the TiO_2 surface as well as the larger Pd nanoparticles, which is confirmed by EDS mapping of the spent catalyst 5 (Fig. S4†). It has been known that the morphology of the nanoparticle can be affected by both the time for particle-particle collisions and the time for inter-particle coalescence.[25] When the time for particle-particle collisions is larger

Table 2 Fractions of metallic Pd, PdO and intermediate PdO_x as determined from XPS analysis, masses of metallic Pd ($M_{metallic\ Pd}$), PdO (M_{PdO}) and intermediate PdO_x (M_{PdO_x}), and total surface area of metallic Pd ($TSA_{metallic\ Pd}$), PdO (TSA_{PdO}) and intermediate PdO_x TSA_{PdO_x}).

	Metallic Pd (%)	PdO (%)	PdO_x (%)	$M_{metallic\ Pd}$ (μg)	M_{PdO} (μg)	M_{PdO_x} (μg)[a]	$TSA_{metallic\ Pd}$ (cm^2)	TSA_{PdO} (cm^2)	TSA_{PdO_x} (cm^2)[b]
catalyst 1	33.34 ± 1.23	32.83 ± 3.44	33.83 ± 2.19	8.00	9.06	8.72	-	-	-
catalyst 2	34.93 ± 2.70	32.75 ± 1.19	32.32 ± 1.51	15.82	17.07	15.74	156.44	241.91	183.37
catalyst 3	42.32 ± 4.01	26.35 ± 3.09	31.34 ± 1.92	32.14	23.02	25.59	245.56	252.17	230.37
catalyst 4	36.40 ± 1.89	28.07 ±1.03	35.52 ± 0.90	39.28	34.85	41.21	233.01	296.35	288.03
catalyst 5	35.78 ± 2.89	25.26 ± 4.80	38.96 ± 1.91	44.81	36.39	52.46	217.26	252.97	299.68

[a] The molecular weight of PdO_x was assumed to be the average of the molecular weights of the metallic Pd and PdO.
[b] The density of PdO_x was assumed to be the average of the densities of the metallic Pd and the PdO.

than the time for inter-particle coalescence, the particle coalesces before it collides with another particle, which results in the larger spherical particle. In the opposite case, the particle collides with another particle before it coalesces, which causes the aggregates of the particles.[25] In this study, with the largest Pd loading (catalyst 5), the Pd nanoparticles could have more opportunity to collide with other Pd nanoparticles on the TiO_2 surface. Thereby, the time for colliding can be smaller than the time for inter-particle coalescence, resulting in the aggregates of Pd nanoparticles on the TiO_2 surface (the third column of Fig. 2c). It should be noted that the size of non-spherical aggregates of Pd particles was excluded and not used for further calculation in the following sections.

Distinguishing oxidation states of components in fresh and spent catalysts (XPS). To investigate the effect of different Pd loadings on the Pd species in the synthesized Pd-TiO_2 catalysts, the Pd oxidation state in the fresh catalysts was evaluated by XPS, with the results shown in the left column of Fig. 3, (all spectra found in Fig. S5†), and summarized in Table 2. Three Pd species were identified based on different characteristic Pd $3d_{5/2}$ core level binding energies: metallic Pd (335.7 eV), intermediate PdO_x (0<x<1) (336.42 eV), and PdO (337.4 eV).[18, 26] Pd species in the XPS data were validated by comparing with those of Pd metal powder (Sigma-Aldrich) and reduced catalyst 3 (see Fig. S6† and additional explanation under Fig. S6†). The XPS spectra confirm that all the Pd-TiO_2 catalysts contained three Pd species, but the percentages of the three Pd species changed as the Pd loading changed. The amount of metallic Pd increased from 33.34 ± 1.23% to 42.32 ± 4.01% as Pd loading was increased from 0.24 wt% to 0.76 wt% (catalyst 1 to catalyst 3). The amount of metallic Pd decreased to 35.78 ± 2.89% as Pd loading was further increased to 1.25 wt% (catalyst 5). On the other hand, the amounts of intermediate PdO_x and PdO showed opposite trends to that of metallic Pd. As mentioned earlier in the section of Flame synthesis of the catalysts and their structures' characterization, the extent of the oxidation of Pd could be varied with different Pd loadings at the same flame-synthesizing condition. The results with the fresh catalysts here are in line with this hypothesis. To study the change in the Pd species at the high temperature under the same experimental condition, the Pd oxidation state in the spent catalysts was also characterized by XPS, and the results are shown in the right column of Fig. 3, (all spectra found in Fig. S3†), and Table S2†. The spent catalysts also contained three Pd species. Compared to the fresh catalysts, the proportions of metallic Pd and PdO_x were increased, while the percentage of PdO was decreased as the Pd loading was increased. Previous studies revealed that the Pd^{2+} was reduced into Pd^0 and/or Pd^+ at the high temperature during methane oxidation reaction.[13, 18] Our analytical results were consistent with these previous findings.

Furthermore, the changes in other species, Ti and O, were evaluated by XPS for both the fresh and the spent catalysts, and the results are shown in Fig. S7†, S8†, Table S3†, and Table S4†. The Ti 2p spectra in both fresh and spent catalysts were deconvoluted into four peaks at approximately 456.7 eV, 458.5 eV, 460.3 eV, and 464.2 eV, which are denoted as Ti^{3+} ($2p_{3/2}$), Ti^{4+} ($2p_{3/2}$), Ti^{3+} ($2p_{1/2}$), and Ti^{4+} ($2p_{1/2}$).[27, 28] This observation implies that Ti in both fresh and spent catalysts was mainly in TiO_2 phase, and the small amount of Ti was in Ti_2O_3 (Ti^{3+}) phase. Compared to the fresh catalysts, an increasing amount of Ti^{3+} was obtained. In addition, the percentage of Ti^{3+} was slightly decreased as the Pd loading was increased. These findings demonstrate the slight phase transformation of TiO_2 toward Ti_2O_3 and the suppressing effect of Pd on the phase transformation, which were matched with the XRD results in the section of Distinguishing crystallinities of the catalysts and phase transformation (XRD). It should be noted that the intensity of Ti was not different much among samples. For comparison, the XPS spectra of O is in both fresh and spent catalysts are shown in Fig. S8† and Table S4†. The XPS spectra of both fresh and spent catalysts showed three noticeable peaks, at approximately 529.9 eV, 531.3 eV, and 532.2 eV, which can be assigned respectively to (1) lattice oxygens in a fully-coordinated environment with metal ions ($O_{lattice}$), (2) oxygen deficient regions of the metal oxide ($O_{deficient\ region}$), and (3) adsorbed oxygen species, such as O_2, H_2O, or M(metal)-OH on the surface,[29] which might be produced during the catalyst synthesis process. We can term these species intrinsically adsorbed oxygen, or $O_{adsorbed}$. There was no significant change in $O_{lattice}$ in the fresh and spent catalysts. On the other hand, an increasing amount of $O_{deficient\ region}$ and a decreasing amount of $O_{adsorbed}$, which indicates the desorption of the adsorbed oxygen species at high temperature and the reduction of Ti and/or Pd.

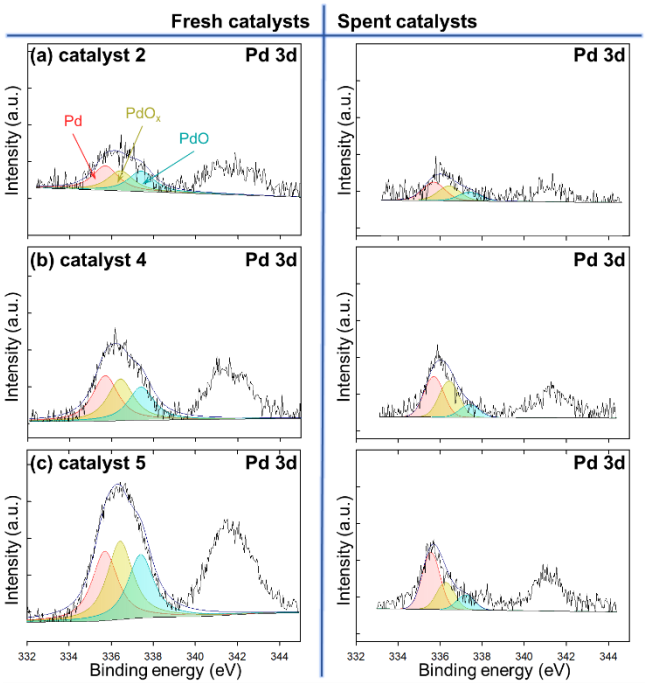

Fig. 3 XPS spectra of fresh and spent Pd-TiO_2 catalysts: Pd metal (red, 335.7 eV), PdO_x (gold, 336.42 eV), PdO (green, 337.4 eV).

In the previous sections and this section, it was confirmed that (1) most Pd was deposited on the TiO_2 surface, (2) size of Pd-TiO_2 was not changed much, and (3) the intensity of Ti was not different much among fresh and spent catalysts. Based on these results, the dispersion or sintering of Pd on the TiO_2 surface can be determined by comparing the ratio between the intensity of Pd 3d (I(Pd)) and Ti 2p (I(Ti)) in fresh and spent catalysts. The ratios were calculated, and they were compared (Table S2†). The calculated values were decreased as the Pd loading was increased, which could imply the decreased Pd coverage on the TiO_2 surface due to sintering of Pd.

This is consistent with our STEM and XRD results showing the increasing size of Pd.

Total surface area of different Pd species. Based on the $M_{Total\ Pd}$ (Table 1) and XPS analytical results, the masses of metallic Pd ($M_{metallic\ Pd}$), PdO (M_{PdO}) and intermediate PdO_x (M_{PdO_x}) were calculated by

$$M_{metallic\ Pd}\ (\mu g) = M_{Total\ Pd} \times \frac{Metallic\ Pd\ (\%)}{100}, \quad (1)$$

$$M_{PdO}\ (\mu g) = M_{Total\ Pd} \times \frac{PdO\ (\%)}{100} \times \frac{MW_{PdO}}{MW_{Pd}}, \quad (2)$$

$$M_{PdO_x}\ (\mu g) = M_{Total\ Pd} \times \frac{PdO_x\ (\%)}{100} \times \frac{MW_{PdO_x}}{MW_{Pd}}, \quad (3)$$

where MW_{Pd}, MW_{PdO} and MW_{PdO_x} represent the molar weights of Pd, PdO and PdO_x, respectively. It should be noted that most Pd subnano-clusters/nanoparticles were distributed on the catalyst's surface, which was demonstrated by ICP-MS and FESEM-EDS. Therefore, XPS analytical results could be combined here to calculate the masses of different Pd phases. MW_{PdO_x} was assumed to be an average of MW_{Pd} and MW_{PdO}. The calculated values based on the fresh catalysts are summarized in Table 2, showing that the mass of each Pd species does not depend on the fraction of Pd species, but instead depends on the Pd loading. The total surface area (TSA) of each Pd species was further calculated based on

$$M\ (\mu g) = N \times \frac{\pi}{6} \times d^3 \times \rho, \quad (4)$$

$$TSA\ (cm^2) = \frac{6M}{\rho d} = N \times \pi \times d^2, \quad (5)$$

where N, d, and ρ represent the number, diameter, and density of each Pd species, respectively. For the calculation, the Pd species were assumed to have the same size and spherical shape of Pd subnano-clusters/nanoparticles, and an average density of metallic Pd and PdO was used for the density of PdO_x. Because of different masses and densities of the three different Pd species, different volumes and areas of them were expected. The calculated values are summarized in Table 2. It is worth noting that the $\boldsymbol{TSA}$ values of metallic Pd, PdO and PdO_x show different trends. $\boldsymbol{TSA_{metallic\ Pd}}$ increases with increasing Pd loading (catalyst 2 to 3) and reaches the largest value of 245.56 cm^2. Then, it decreases as the Pd loading is further increased (catalyst 3 to 5). In the case of $\boldsymbol{TSA_{PdO}}$, a similar trend is found, but the peak value of 296.35 cm^2 is found with catalyst 4. The $\boldsymbol{TSA_{PdO_x}}$ increases with increasing Pd loading (catalyst 2 to 5) and reaches its largest value of 299.68 cm^2 with the highest Pd loading (catalyst 5). However, for any Pd phase (metallic Pd, PdO and PdO_x), the sample-by-sample $\boldsymbol{TSA}$ dependence exhibits the same trend as the percentage of this phase. In the case of the spent catalysts, the comparison was done among catalysts 2, 3 and 4, and the results are shown in Table S2†. According to STEM analytical results, there were aggregates of Pd nanoparticles in the spent catalyst 5, and thereby the calculation based on the spherical shape of primary Pd particles could not be applied. In Table S2†, $\boldsymbol{TSA_{metallic\ Pd}}$ of the spent catalysts followed a similar trend to $\boldsymbol{TSA_{metallic\ Pd}}$ of the fresh catalysts: $\boldsymbol{TSA_{metallic\ Pd}}$ was increased

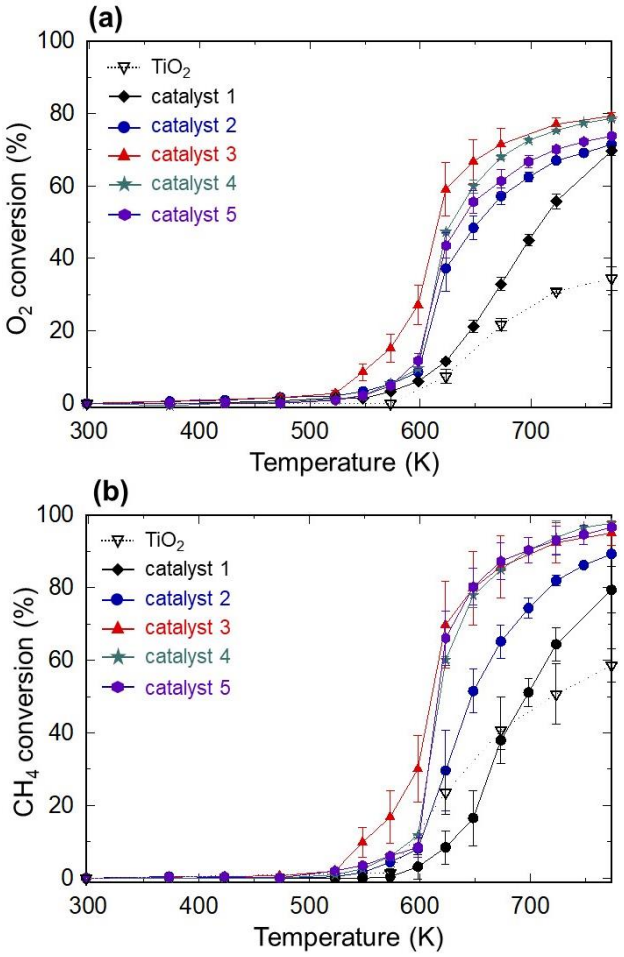

Fig. 4 (a) O_2 and (b) CH_4 conversion vs. temperature with TiO_2, catalyst 1, catalyst 2, catalyst 3, catalyst 4, and catalyst 5.

from 85.68 cm^2 to 124.70 cm^2 as the Pd loading was increased (catalyst 2 to 3), and then it was decreased to 105.61 cm^2 as the Pd loading was further increased (catalyst 3 to 4). On the other hand, unlike the fresh catalysts, $\boldsymbol{TSA_{PdO}}$ and $\boldsymbol{TSA_{PdO_x}}$ of the spent catalysts show a similar trend to $\boldsymbol{TSA_{metallic\ Pd}}$ of the spent catalysts: Both were increased to 70.78 cm^2 and 131.74 cm^2 as the Pd loading was increased from catalyst 2 to catalyst 3, and further decreased to 64.75 cm^2 and 120.12 cm^2 as the Pd loading was increased to catalyst 4. It should be noted that all *TSA* of the spent catalysts were smaller than those of the fresh catalysts because Pd subnano-clusters/nanoparticles were sintered on the TiO_2 surfaces at the high temperature. The $\boldsymbol{TSA}$ of metal could play a crucial role in the catalytic activity by providing active sites for the reaction, and thus higher catalytic activity is expected with the larger $\boldsymbol{TSA}$ of metal. Because the $\boldsymbol{TSA}$ of all Pd species showed different trends, the important Pd species on the catalytic activity in O_2 removal could be demonstrated, which is discussed in the following section.

Catalytic activity of the synthesized Pd-TiO_2 catalysts in O_2 removal

Catalytic activity evaluation in O_2 removal. The synthesized Pd-TiO_2 catalysts were evaluated for O_2 removal. The experiments were conducted under initial O_2 rich composition ($O_2/CH_4 \cong 2.4$, ~1.45% of CH_4), with excessive CO_2 (~95%) as the balance of the gas. The experiments under other initial conditions are shown in the following

section of Influence of reactants and products. The O_2 and CH_4 conversions were calculated based on:

$$\text{Conversion}\ (\%) = \frac{C_i - C_f}{C_i} \times 100, \quad (6)$$

where $\boldsymbol{C_i}$ and $\boldsymbol{C_f}$ represent the initial and final concentrations of gas, respectively. Data on "conversion-temperature" dependencies are presented in Fig. 4 and Table S5†.

All reactants and products were analyzed by using a GC. The concentrations of both O_2 and CH_4 decreased as the temperature was increased. CO_2 gas was detected, but in our typical experiment the CO_2 concentration was comparatively high, and its change was hard to monitor. On the other hand, there was no CO and H_2 observed. To confirm the generation of CO_2 as a product and the major reaction, a separate experiment was performed with He gas as the balance of the gas instead of CO_2, with the results shown in Fig. S6†. Decreasing trends were found in the O_2 and CH_4 concentrations. Only CO_2 (no CO) was observed as a product, and the total concentration of C remained constant during the reaction. Furthermore, the reaction rate of CH_4 is half the reaction rate of O_2 via complete CH_4 oxidation reaction ($CH_4 + 2O_2 \rightarrow CO_2 + 2H_2O$) ($R_{CH_4} = 1/2R_{O_2}$). The reaction rate of both CH_4 and O_2 at 723 K and 773 K were summarized in Table S5†. Table S6† indicates stoichiometry: the reaction rates of CH_4 are close to the half of the reaction rates of O_2 at both 723 K and 773 K ($\left|\frac{R_{CH_4} - \frac{1}{2R_{O_2}}}{R_{CH_4}}\right| \times 100 \leq 6\ \%$). Therefore, complete CH_4 oxidation was the single overall reaction in this system. In addition, there was no CO_2 generation without O_2, which confirmed that CO_2 generation was not from the catalyst body, but from the provided O_2 stream. All catalysts showed the same trends of reactant and product concentrations.

Fig. 4 and Table S5† show an enhanced O_2 and CH_4 conversions with Pd-TiO_2 catalysts compared to those with only TiO_2 (~30.9% for O_2, and ~50.7% for CH_4 at 723 K). This result emphasizes the importance of Pd in effective O_2 removal. In addition, O_2 conversion increased from 55.8% to 77.0% at 723 K with increasing Pd loading (catalyst 1 to 3). However, it decreased when the Pd loading was further increased (catalyst 3 to 5). This volcano-shaped dependency could imply that total Pd loading might be insufficient to reveal the active phase of Pd for the O_2 removal reaction. Because different Pd species (metallic Pd, PdO and PdO_x) could participate in the reaction, it is necessary to perform special studies for understanding the relationship between the reaction rate and the active phase of Pd. It is described in the next section. CH_4 conversion was enhanced from 64.4% to 92.4% as Pd loading was increased (catalyst 1 to 3), and then no significant difference was observed as Pd loading was further increased.

Apparent reaction rate constant and total surface area of Pd species. Our preliminary experiments at different temperatures proved that the O_2 removal reaction with Pd-TiO_2 catalysts followed an apparent first order reaction (R^2>0.92) in Fig. S10†. Therefore, the apparent reaction rate constant (k_{app}) can be determined by

$$\frac{dC}{d\tau} = -k_{app}C, \quad (7)$$

where C and τ represent the concentration of O_2 and residence time (min). The calculated k_{app} values at 723 K are summarized in Table S5†. It should be noted that when the plot of k_{app} and the total Pd loading was expressed (Fig. 5a), an optimal total Pd loading was observed. A similar volcano-shape of the reaction rate of CH_4 with the size of Pd was widely observed and one example can be found in the previous study by Willis et al.[30] Because different Pd species (metallic Pd, PdO and PdO_x) could be involved in the O_2 removal reaction, the relationship between k_{app} and total Pd loading might not be sufficient to understand the active phase of Pd for the reaction. To reveal the active phase of Pd, it is necessary to distinguish the contributions of different Pd species on the O_2 removal reaction. Also, it must be understood the change in the catalytic properties during the reaction and corresponding catalytic activity. In the interpretation of kinetic data, the hypothesis of additivity can be formulated. In accordance with this hypothesis, the reaction occurs on different Pd phases (i.e., metallic Pd, PdO and PdO_x). Previously, Kannisto et al. and Murzin[31, 32] analyzed contributions of different geometric sites into the whole catalytic activity. Similar to their additive approach, k_{app} can be presented as a sum of different contributions:

$$k_{app} = k_{app,metallid\ Pd}\alpha + k_{app,PdO}\beta + k_{app,PdO_x}\gamma, \quad (8)$$

$$\alpha = \frac{TSA_{metallic\ Pd}}{TSA_{total}}, \beta = \frac{TSA_{PdO}}{TSA_{total}}, \gamma = \frac{TSA_{PdO_x}}{TSA_{total}}, \quad (9)$$

$$\alpha + \beta + \gamma = 1, \quad (10)$$

where $k_{app,metallic\ Pd}$, $k_{app,PdO}$ and k_{app,PdO_x} represent the apparent reaction rate constants on metallic Pd, PdO and PdO_x, respectively. The obtained k_{app} is presented as a function of fractions of the total surface area of each Pd species (α, β and γ). In this study, three different types of α, β and γ were obtained based on the analytical results of (1) fresh and (2) spent catalysts, and (3) averages of them: α_{fresh}, β_{fresh} and γ_{fresh} represent the fraction of the total surface area of metallic Pd, PdO and PdO_x, respectively, and those in the spent catalysts were denoted as α_{spent}, β_{spent} and γ_{spent}, respectively. In addition, α_{avg}, β_{avg} and γ_{avg} were obtained by averaging the analytical results of fresh and spent catalysts. The relationships between the calculated k_{app} and α, β and γ were further investigated: The plots of k_{app} and fractions in the fresh catalysts (α_{fresh}, β_{fresh} and γ_{fresh}) were expressed with temperatures near at which the catalytic activity was initiated. The plots of k_{app} and fractions in the spent catalysts (α_{spent}, β_{spent} and γ_{spent}) were displayed with the high temperatures. The moderate temperatures were used for the plots of k_{app} and average fractions (α_{avg}, β_{avg} and γ_{avg}) as well. In the case of the fresh catalysts, a linear increase was observed with k_{app} and α_{fresh} (metallic Pd) (R^2>0.91) (Fig. 5b), while as for the dependencies between k_{app} and β_{fresh} (PdO) and between k_{app} and γ_{fresh} (PdO_x), no correlation was found (Fig. S11†). Therefore, it can be concluded that for the fresh catalysts, the apparent catalytic activity is governed by metallic Pd and the contribution of Pd oxides is insignificant.

In the cases of the spent catalysts and the averaged values, like the plot of $\boldsymbol{k_{app}}$ and $\boldsymbol{\alpha_{fresh}}$ (metallic Pd), $\boldsymbol{k_{app}}$ was generally linearly increased as both $\boldsymbol{\alpha_{spent}}$ and $\boldsymbol{\alpha_{avg}}$ were increased with R^2>0.85 and R^2>0.90, respectively (Fig. S12†). No correlations between $\boldsymbol{k_{app}}$ and $\boldsymbol{\gamma_{spent}}$ (PdO_x) and between $\boldsymbol{k_{app}}$ and $\boldsymbol{\gamma_{avg}}$ were observed (Fig. S13†).

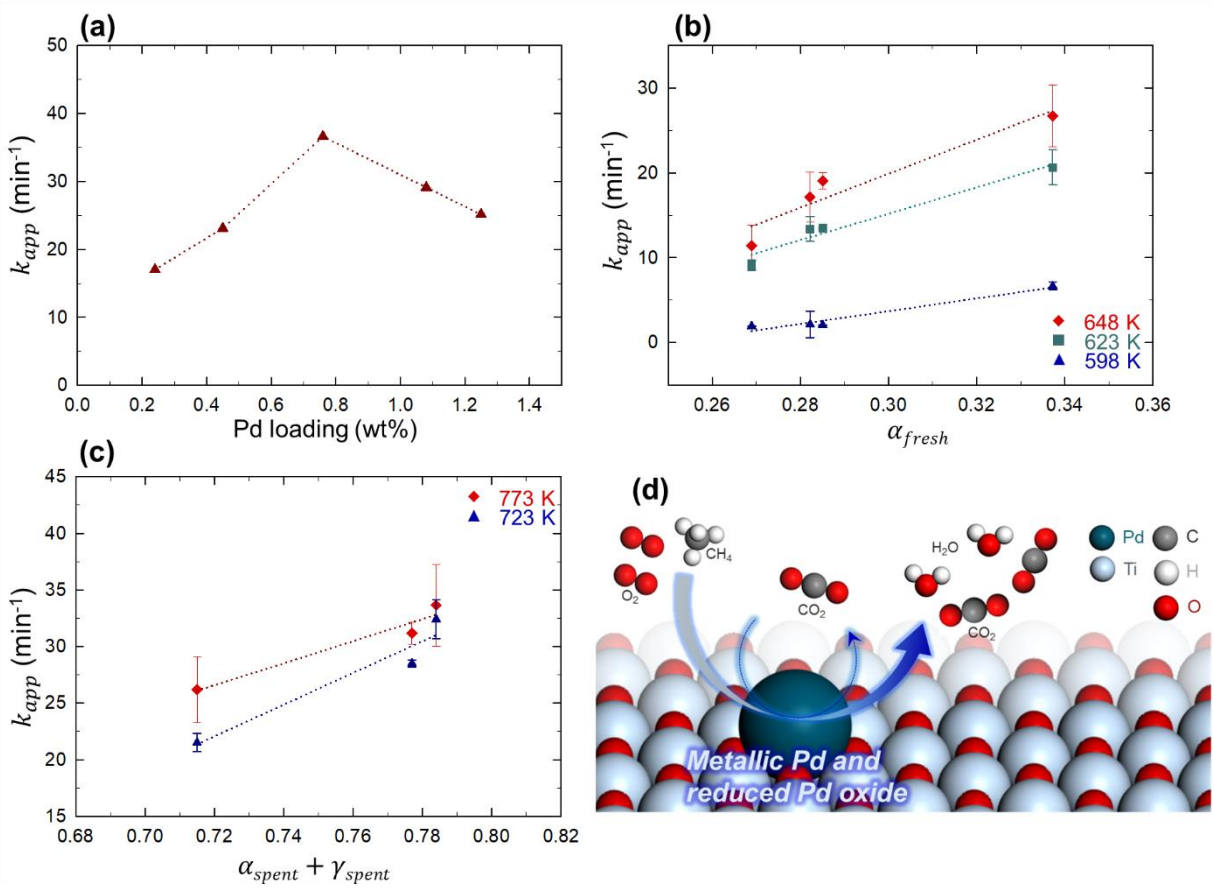

Fig. 5 (a) Variation of the apparent reaction rate constant (k_{app}) with (a) Pd loading, (b) the fraction of the total surface area of metallic Pd in the fresh catalysts (α_{fresh}), (c) the sum of the fractions of the total surface area of metallic Pd and PdO_x in the spent catalysts ($\alpha_{spent} + \gamma_{spent}$), and (d) schematic diagram of O_2 removal by using flame-synthesized Pd-TiO_2 catalyst.

It is interesting to note that unlike the plot of $\boldsymbol{k_{app}}$ and $\boldsymbol{\beta_{fresh}}$ (PdO), $\boldsymbol{k_{app}}$ was linearly decreased as both $\boldsymbol{\beta_{spent}}$ and $\boldsymbol{\beta_{avg}}$ were increased (Fig. S14†). These results could indicate the metallic Pd is the active catalytic phase. However, it is risky to conclude that only metallic Pd plays a crucial role in the reaction. The catalysts generally go through a complex process during the reaction in which Pd oxides are partially reduced to metallic Pd or/and PdO_x ($0<x<1$) species, experimentally distinguished (see previous section of Distinguishing oxidation states of components in fresh and spent catalysts (XPS)). The calculated $\boldsymbol{k_{app}}$ exhibited the linear dependence regarding the combined fractions of the total surface area of metallic Pd and PdO_x ($\boldsymbol{\alpha_{spent} + \gamma_{spent}}$ and $\boldsymbol{\alpha_{avg} + \gamma_{avg}}$) (Fig. 6c and Fig. S15†). The results based on the current calculations may contain a systematic error because the cross-section difference between Pd species was not taken into the calculations and the role of the interface between Pd particles and TiO_2 surface was not considered. However, we note that our finding from the current calculations was consistent with the previous studies by Yang et al.[13] and Murata et al.[14]: The previous study by Yang et al.[13] reported the reduced form of Pd (Pd^0 and PdO_x ($0<x<1$)) was preferential for the effective methane oxidation reaction. The recent study by Murata et al.[14] described the important role of the mixed phases of Pd and Pd oxide in the methane oxidation reaction. A theoretical study by using density functional theory (DFT) calculations also revealed the lower activation energy barrier for methane decomposition, which is widely accepted as the reaction rate limiting step, on the reduced PdO surface.[33] Therefore, it could be concluded that metallic Pd mainly controls the O_2 removal reaction and the reduced Pd phase, metallic Pd or/and PdO_x, at high temperature also generates an active phase for the reaction (Fig. 5d). Our interpretation of results of physico-chemical analysis and kinetic studies emphasizes that the Pd loading itself does not affect the intrinsic catalytic property of the synthesized catalyst, but the fraction of active Pd phases, which are metallic Pd or/and reduced Pd (PdO_x), significantly determines it. A linear dependency between the $\boldsymbol{k_{app}}$ and the fraction of the total surface area of active Pd phases (metallic Pd or/and reduced form of Pd) results in the constant catalytic activity per unit area of metallic Pd or/and reduced form of Pd. Calculated apparent turnover frequencies of catalyst 3 to 5 were close each other (~8×10^{-4} mmol hr^{-1} cm^{-2}). It means that we observe the case of so-called structure insensitive catalytic system defined by Boudart.[34] For such systems, the catalytic activity per unit of area is related to the specific active component and does not depend on the preparation method providing a guidance for the catalyst design.[34-36] Also, the negative effect of water on the CH_4 oxidation reaction has been widely studied, and it correlates to the structure of Pd.[37, 38]

Influence of reactants and products. The previous experiments were conducted under O_2 rich composition ($O_2/CH_4 \cong 2.4$). In this section, two different initial compositions were considered: first, different CO_2 concentrations (0% and 53%, He as the balance of the gas) under O_2 rich composition in the initial gas stream were applied. Second, different ratios between O_2 and CH_4 concentrations

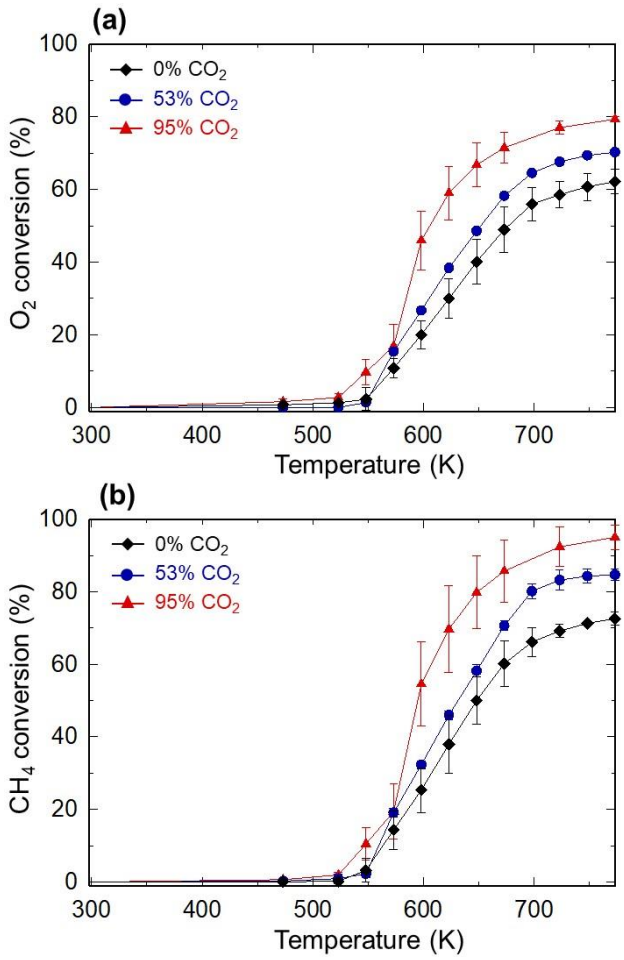

Fig. 6 (a) O_2 and (b) CH_4 conversion vs. temperature with catalyst 3 under different initial compositions (0%, 53%, and 95% of CO_2 in balance He).

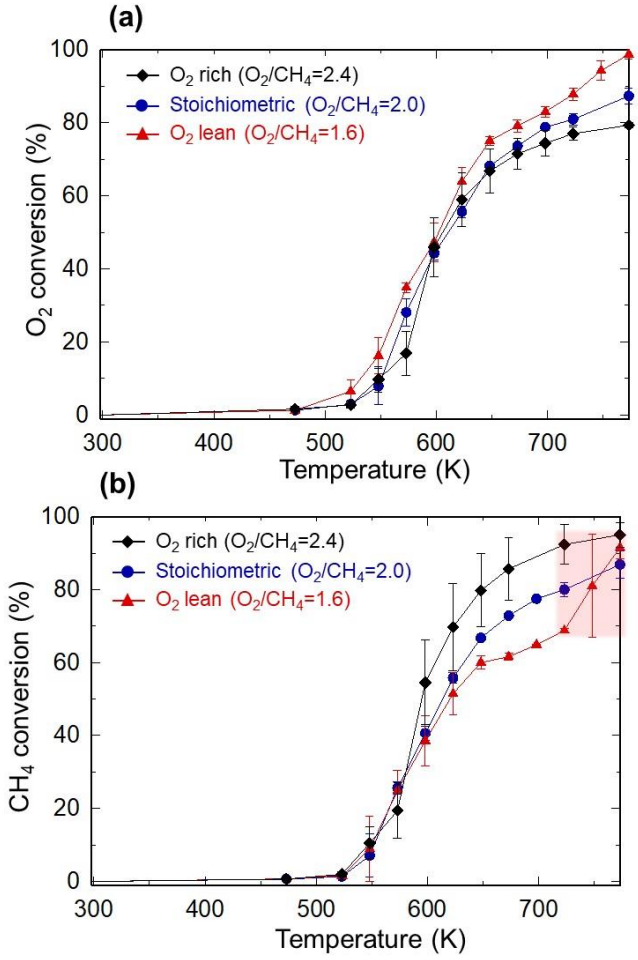

Fig. 7 (a) O_2 and (b) CH_4 conversion vs. temperature with catalyst 3 under different initial compositions (O_2 rich composition: $O_2/CH_4 \cong 2.4$, stoichiometric composition: $O_2/CH_4 \cong 2.0$, O_2 lean composition: $O_2/CH_4 \cong 1.6$).

(stoichiometric composition: $O_2/CH_4 \cong 2.0$ and O_2 lean composition: $O_2/CH_4 \cong 1.6$ with excessive CO_2 as the balance of the gas) were tested.

To investigate the effect of CO_2 concentration in the initial gas stream on the O_2 removal, experiments with different CO_2 concentrations (0% and 53%, He as the balance of the gas) under O_2 rich composition ($O_2/CH_4 \cong 2.4$, ~1.45% of CH_4) were conducted, and their results and the previous result with 95% of CO_2 are shown in Fig. 6. Complete CH_4 oxidation was the main reaction between CH_4 and O_2, which was proved by the closed values between the reaction rates of CH_4 and the half of reaction rates of O_2 (Table S7†). It should be noted that both O_2 and CH_4 conversions were enhanced as the CO_2 concentration was increased. The plot between the O_2 reaction rate versus the initial CO_2 concentration in Fig. S16† shows that the O_2 conversion rate (mmol g_{cat}^{-1} hr^{-1}) versus the concentration of initial CO_2 (mol m^{-3}) at different temperatures could be approximately explained by a linear dependence (R^2>0.88). It may be explained by an autocatalytic effect of CO_2 or a coverage effect of CO_2. Previously, the autocatalytic effect on different applications has been reported and the accelerated reaction rates were mostly supported by the lower activation energy via new intermediates (e.g. new CO_2-bonded intermediates).[39, 40] On the other hand, the coverage effect of surface species on various applications have been also reported in previous studies.[41, 42] The lower activation energy was reported with surface coverages of gas molecules due to the modification of the surface electronic structure.[41, 42] According to these previous studies, it could be assumed that CO_2 is itself involved in the O_2 removal reaction and causes the enhanced reaction rate via the autocatalytic effect of the surface coverage effect (Fig. 5d). The application of DFT calculations will be useful for understanding these effects.

Results under second initial composition were compared with the previous one which was performed under O_2 rich composition with excessive amount of CO_2 as the balance of the gas (95%) in Fig. 7. Fig. 7 demonstrates: as the ratio between O_2 and CH_4 was decreased from the O_2 rich composition to the O_2 lean one, the conversion of O_2 was increased. This result indicates that more reaction source (CH_4) can enhance the O_2 conversion. It should be also noted that there was a sharp increase in the CH_4 conversion at around 723 K under O_2 lean condition (Fig. 7b). This sudden increase in the CH_4 conversion could be due to the CO generation at high temperature (Fig. S17†). A previous study reported the same trend which shows the decreasing CO_2 selectivity due to the formation of CO under O_2 lean composition $O_2/CH_4 \cong 1.5$ and 1.75).[11] This

experimental result implies that excessive CH_4 could cause a nonpreferred reaction product.

Conclusions

Pd-TiO_2 catalysts with varying Pd loading were synthesized by using a flame aerosol reactor, and the material and kinetic characteristics of the fresh catalysts and spent catalysts were evaluated. Our study contributes to three major findings: (1) In the case of the fresh catalysts, the addition of Pd did not change the crystal structure and the size of the Pd-TiO_2 particle, but the size of Pd subnano-clusters/nanoparticles and the oxidation state of Pd (metallic Pd, PdO and PdO_x) was affected by Pd loading. In the case of the spent catalysts, increased size of Pd nanoparticles on the catalyst's surface was observed due to the sintering effect. With the highest Pd loading, aggregates of Pd nanoparticles on the catalyst's surface were obtained. Also, some amount of PdO was reduced to either metallic Pd or intermediate PdO_x. (2) The total surface areas of different Pd species in the fresh and spent catalysts were evaluated based on the size distribution of Pd and fractions of Pd species. For the fresh catalysts, the apparent reaction rate constants were proportional to the calculated fraction of the total surface area (TSA) of metallic Pd. For the spent catalysts, a linear correlation between the apparent reaction rate constants and the combined fraction of TSA (metallic Pd and reduced Pd oxide, i.e. PdO_x ($0<x<1$)) was obtained as well. Different catalytic characteristics on Pd loading exhibit the volcano-shaped dependencies. However, behind these dependencies, a linear proportionality between apparent kinetic constants and fractions of total surface areas of metallic Pd or/and reduced Pd oxide is revealed using distinguishing different Pd phases, which represents the intrinsic activity of the active site. (3) CO was generated at high temperature under O_2 lean condition. And the reaction rate of O_2 had a linear dependency on the initial CO_2 concentration, which could be explained by an autocatalytic effect or a surface coverage effect. This study provides structural and kinetic investigation on O_2 removal with flame-synthesized Pd-TiO_2 catalysts and emphasizes the kinetic role of metallic Pd and reduced Pd oxide. This study also proposed a positive effect of initial CO_2 concentration on O_2 removal. Detailed role of the excessive amount of CO_2 in the feed stream on O_2 removal will be addressed in our further study.

Conflicts of interest

There are no conflicts to declare.

Acknowledgements

This work was supported by a grant funded by the U.S. Department of Energy's National Energy Technology Laboratory under Award Number DE-FE0029161.

References

1. B. J. P. Buhre, L. K. Elliott, C. D. Sheng, R. P. Gupta and T. F. Wall, *Prog. Energ Combust.,* 2005, **31**, 283-307.
2. M. Kanniche, R. Gros-Bonnivard, P. Jaud, J. Valle-Marcos, J. M. Amann and C. Bouallou, *Appl. Therm. Eng.,* 2010, **30**, 53-62.
3. S. Chu, *Science*, 2009, **325**, 1599-1599.
4. Z. Dai, R. Middleton, H. Viswanathan, J. Fessenden-Rahn, J. Bauman, R. Pawar, S. Y. Lee and B. McPherson, *Environ. Sci. Technol. Lett*, 2014, **1**, 49-54.
5. DOE/NETL. Quality guidelines for energy system studies: CO_2 impurity design parameters. 2013.
6. P. Gélin and M. Primet, *Appl. Catal. B*, 2002, **39**, 1-37.
7. P. Gelin and M. Primet, *Appl Catal B-Environ*, 2002, **39**, 1-37.
8. A. I. Osman, J. K. Abu-Dahrieh, F. Laffir, T. Curtin, J. M. Thompson and D. W. Rooney, *Appl. Catal. B*, 2016, **187**, 408-418.
9. K. Muto, N. Katada and M. Niwa, *Appl. Catal. A*, 1996, **134**, 203-215.
10. Q. Zheng, S. Zhou, M. Lail and K. Amato, *Ind. Eng. Chem. Res.*, 2018, **57**, 1954-1960.
11. A. N. Kuhn, Z. Chen, Y. Lu and H. Yang, *Energy Technol.*, 2019, **7**, 1800917.
12. M. Schmal, M. M. V. M. Souza, V. V. Alegre, M. A. P. da Silva, D. V. César and C. A. C. Perez, *Catal. Today*, 2006, **118**, 392-401.
13. S. Yang, A. Maroto-Valiente, M. Benito-Gonzalez, I. Rodriguez-Ramos and A. Guerrero-Ruiz, *Appl. Catal. B*, 2000, **28**, 223-233.
14. K. Murata, D. Kosuge, J. Ohyama, Y. Mahara, Y. Yamamoto, S. Arai and A. Satsuma, *ACS Catal.*, 2019, **10**, 1381-1387.
15. F. Ortloff, J. Bohnau, F. Graf and T. Kolb, *Appl. Catal. B*, 2016, **182**, 375-384.
16. Z. M. Wang, G. Yang, P. Biswas, W. Bresser and P. Boolchand, *Powder Technol.*, 2001, **114**, 197-204.
17. V. Tiwari, J. Jiang, V. Sethi and P. Biswas, *Appl. Catal. A*, 2008, **345**, 241-246.
18. F. Niu, S. Li, Y. Zong and Q. Yao, *J. Phys. Chem. C.*, 2014, **118**, 19165-19171.
19. R. Strobel, S. E. Pratsinis and A. Baiker, *J. Mater. Chem. C*, 2005, **15**, 605-610.
20. K. Fujiwara and S. E. Pratsinis, *AIChE J.*, 2017, **63**, 139-146.
21. W. N. Wang, W. J. An, B. Ramalingam, S. Mukherjee, D. M. Niedzwiedzki, S. Gangopadhyay and P. Biswas, *J. Am. Chem. Soc.*, 2012, **134**, 11276-11281.
22. R. Gholami, M. Alyani, K. J. Smith, *Catalysts*, 2015, **5**, 561-594.
23. C. H. Bartholomew, *Appl. Catal. A*, 2001, **212**, 17-60.
24. A. W. Petrov, D. Ferri, F. Krumeich, M. Nachtegaal, J. A. van Bokhoven, O. Kröcher, *Nat. Commun.*, 2018, **9**, 2545.
25. P. Gelin and M. Primet, *Appl Catal B-Environ*, 2002, **39**, 1-37.
26. J. J. Willis, E. D. Goodman, L. Wu, A. R. Riscoe, P. Martins, C. J. Tassone and M. Cargnello, *J. Am. Chem. Soc.*, 2017, **139**, 11989-11997.
27. B. M. Kumfer, K. Shinoda, B. Jeyadevan and I. M. Kennedy, *J. Aerosol Sci.*, 2010, **41**, 257-265.
28. Y. Zhong, C. Yue, B. Chen, S. Sun, M. Zheng, L. Zhao, S. Wu, J. Li, J. Kang and L. Lin, *RSC Adv.*, 2015, **5**, 37399-37404.

29. S. Q. Li, Y. H. Ren, P. Biswas and S. D. Tse, *Prog. Energ Combust.*, 2016, **55**, 1-59.
30. A. Bin Yousaf, M. Imran, M. Farooq and P. Kasak, *Sci. Rep.*, 2018, **8**.
31. M. N. Ghazzal, R. Wojcieszak, G. Raj and E. M. Gaigneaux, *Beilstein J. Nanotechnol.*, 2014, **5**, 68-76.
32. T. M. Masiala, A. K. M. Bantu, G. E. Bakambo, J. M. Lunguya, J. L. K. Kanza, O. M. Muamba, *International Journal of Materials Science and Applications*, 2016, **5**, 207-213.
33. P. Liu, T. P. Chen, X. D. Li, Z. Liu, J. I. Wong, Y. Liu and K. C. Leong, *Ecs Solid State Lett.*, 2013, **2**, Q21-Q24.
34. J. J. Willis, A. Gallo, D. Sokaras, H. Aljama, S. H. Nowak, E. D. Goodman, L. Wu, C. J. Tassone, T. F. Jaramillo and F. Abild-Pedersen, *ACS Catal.*, 2017, **7**, 7810-7821.
35. H. Kannisto, K. Arve, T. Pingel, A. Hellman, H. Harelind, K. Eranen, E. Olsson, M. Skoglundh and D. Y. Murzin, *Catal. Sci. Technol.*, 2013, **3**, 644-653.
36. D. Y. Murzin, *Catal. Lett.*, 2012, **142**, 1279-1285.
37. A. Hellman, A. Resta, N. M. Martin, J. Gustafson, A. Trinchero, P. A. Carlsson, O. Balmes, R. Felici, R. van Rijn, J. W. M. Frenken, J. N. Andersen, E. Lundgren and H. Grönbeck, *J. Phys. Chem. Lett.*, 2012, **3**, 678-682.
38. A. S. Crampton, M. D. Rötzer, C. J. Ridge, B. Yoon, F. F. Schweinberger, U. Landman and U. Heiz, *Surf. Sci.*, 2016, **652**, 7-19.
39. J. E. Benson, H. W. Kohn and M. Boudart, *J. Catal.*, 1966, **5**, 307-&.
40. G. H. Zhu, J. Y. Han, D. Y. Zemlyanov and F. H. Ribeiro, *J Am Chem Soc.*, 2004, **126**, 9896-9897.
41. W. Huang, E. D. Goodman, P. Losch and M. Cargnello, *Ind. Eng. Chem. Res.*, 2018, **57**, 10261-10268.
42. X. Li, X. Wang, K. Roy, J. A. van Bokhoven and L. Artiglia, *ACS Catal.*, 2020, **10**, 5783-5792.
43. A. E. Masunov, E. Wait and S. S. Vasu, *J. Phys. Chem. A*, 2016, **120**, 6023-6028.
44. Y. Yang, C. A. Mims, D. H. Mei, C. H. F. Peden and C. T. Campbell, *J. Catal.*, 2013, **298**, 10-17.
45. P. Wu and B. Yang, *ACS Catal.*, 2017, **7**, 7187-7195.
46. K. R. Hahn, M. Iannuzzi, A. P. Seitsonen and J. Hutter, *J. Phys. Chem. C*, 2013, **117**, 1701-1711.